# Indian Ocean subtropical dipole simulated using a coupled general circulation model

Rieko Suzuki,[1] Swadhin K. Behera,[2] Satoshi Iizuka,[3] and Toshio Yamagata[1]

Received 21 May 2003; revised 27 May 2004; accepted 14 June 2004; published 1 September 2004.

[1] The interannual Indian Ocean subtropical dipole (IOSD) event in the southern Indian Ocean is discussed using a coupled general circulation model to derive a scenario describing its complete life cycle for the first time. The positive (negative) IOSD is characterized by an anomalous warm (cool) sea surface temperature (SST) in the southwestern region of the Indian Ocean and by an anomalous cool (warm) SST in the southeastern region. The positive event brings about enhanced precipitation in the southeastern Africa during the peak phase. Composite pictures for the positive and negative IOSD clarify that an anomalous latent heat flux is the dominant factor in its formation. This flux anomaly is caused by an anomaly in the climatological wind field, which is associated with a pressure anomaly in the central region of the southern Indian Ocean. Since the flux anomaly starts during austral fall in the year previous to the event peak and develops for the next 9 months, air-sea interaction must play an active role in the formation of the IOSD. The reason the peak of the IOSD is locked to the austral summer is that the latent heat flux influences the sea surface temperature most efficiently in the austral summer when the depth of the surface mixed layer is shallowest. *INDEX TERMS:* 4215 Oceanography: General: Climate and interannual variability (3309); 4255 Oceanography: General: Numerical modeling; 4504 Oceanography: Physical: Air/sea interactions (0312); *KEYWORDS:* Indian Ocean subtropical dipole (IOSD), heat fluxes, air-sea interaction positive feedback

**Citation:** Suzuki, R., S. K. Behera, S. Iizuka, and T. Yamagata (2004), Indian Ocean subtropical dipole simulated using a coupled general circulation model, *J. Geophys. Res.*, *109*, C09001, doi:10.1029/2003JC001974.

## 1. Introduction

[2] *Behera and Yamagata* [2001] (hereafter BY) discussed the interannual occurrence of the Indian Ocean subtropical dipole (IOSD) using observational and reanalysis data sets. The IOSD events are identified as important interannual climate variations in the region. Positive IOSD events are characterized by a warm SST anomaly southeast of Madagascar and a cold SST anomaly west of Australia. These subtropical events are found to have the maxima in the austral summer. Since the data in the region is sparse, we use here simulation results from a coupled general circulation model (CGCM) to examine the subtropical dipole events reported in BY. This is motivated by studies that have already shown the capability of coupled models to simulate extratropical air-sea interaction in the North Pacific and the North Atlantic Oceans. In particular, the North Atlantic Oscillation has been well simulated by several CGCMs [e.g., *Ferreira et al.*, 2001, and references therein].

[3] It has been suggested that the evolution of the IOSD occurs through air-sea interaction in the subtropical Indian Ocean. In BY, it is also shown that the SST anomalies during positive dipole events are related to enhanced moisture over the western warm pole and anomalous rainfall in southern Africa. These atmospheric conditions are simulated by atmospheric general circulation models as a response to those SST anomalies [*Reason and Mulenga*, 1999; *Reason*, 2002]. In addition, in BY, the SST dipole pattern is also associated with the sea level pressure (SLP) anomaly of the Mascarene high. Higher-than-normal pressure during a positive event accompanies stronger winds in the east and weaker winds in the west. These strong winds cause anomalous cooling through enhanced evaporation in the east and the opposite tendency in the west. In this study, we explore the entire IOSD evolution in addition to possible processes that could give rise to the air-sea interaction using a coupled model, which have not clarified before. Such coupled processes in subtropical regions are not well understood compared to those in the tropics.

[4] The rainy season in equatorial east Africa is from October to December and from March to May and in most of southeastern Africa it is from December to February. The El Niño/Southern Oscillation (ENSO) has been put forward as a key element in determining rainfall variability there [*Ropelewski and Halpert*, 1987; *Ogallo et al.*, 1988; *Hastenrath et al.*, 1993; *Allan et al.*, 1996; *Nicholson and*

[1]Department of Earth and Planetary Science, University of Tokyo, Tokyo, Japan.
[2]Institute for Global Change Research/Frontier Research Center for Global Change, Kanagawa, Japan.
[3]National Research Institute for Earth Science and Disaster Prevention, Ibaraki, Japan.


0148-0227/04/2003JC001974$09.00

*Kim*, 1997; *Reason et al.*, 2000]. In recent years, however, the relationship between the rainfall in eastern and southern Africa and surrounding basins (i.e., the Indian Ocean and the Atlantic Ocean) has drawn more attention [*Walker*, 1990; *Mason*, 1995; *Goddard and Graham*, 1999; *Behera and Yamagata*, 2001; *Jury et al.*, 2002; *Saji and Yamagata*, 2003]. In particular, in studies using either observed data (BY) or model results [*Reason and Mulenga*, 1999; *Reason*, 2002], the IOSD influence on southern Africa became clear. In this paper, we also investigate the rainfall pattern associated with the IOSD phenomenon as simulated by the CGCM. We note that the present model, developed at the National Research Institute for Earth and Planetary Science and Disaster Prevention (NIED), was successful in simulating the tropical Indian Ocean Dipole phenomenon [*Iizuka et al.*, 2000] and the associated rainfall variability. In section 2, the details of the CGCM are explained. In section 3, the model climatology is discussed along with observations. In sections 3 and 4, the interannual variability in the subtropics is discussed using a composite technique and a heat budget calculation for each pole of the IOSD. The final section provides a summary.

## 2. Model and Data

[5] The ocean component (OGCM) of the CGCM is based on the Modular Ocean Model 2.2 [*Pacanowski*, 1996], which was developed at the Geophysical Fluid Dynamics Laboratory/National Oceanic and Atmospheric Administration (GFDL/NOAA). This OGCM resolves the global oceans, except for the region north of 70°N, the North Sea, the Mediterranean Sea, the Black Sea, and the Caspian Sea. Because it does not include a sea-ice model, temperature and salinity at the northern and southern boundaries in the CGCM are bound to the climatological values. The model horizontal resolution is 1.125° (longitude) × 0.5625°(latitude). In the vertical, it has 37 levels of which 25 levels are in the upper 400 m. Horizontal mixing is parameterized using a biharmonic scheme, in which the coefficients of horizontal eddy viscosity and diffusivity are fixed at $5 \times 10^{20}$ cm$^4$s$^{-1}$. The vertical mixing parameterization depends on the Richardson number [*Pacanowski and Philander*, 1981]. The penetrative radiation is parameterized with the formula given by *Paulson and Simpson* [1977].

[6] The atmospheric part (AGCM) of the CGCM is a global spectral model derived from a forecast model (GSM8911) developed at the Japan Meteorological Agency (JMA). The model has the triangular truncation at wave number T106 (∼110 km) and 21 levels in the vertical from the surface to 10 hPa level. The hybrid vertical coordinate uses sigma coordinates in the troposphere and isobaric coordinates in the stratosphere. The AGCM contains the following physical parameterizations: long-wave radiation [*Katayama*, 1972; *Sugi et al.*, 1990], short-wave radiation [*Lacis and Hansen*, 1974], surface fluxes [*Louis et al.*, 1982], deep convection [*Kuo*, 1974], and shallow convection [*Tiedtke*, 1985]. A detailed description of the physical processes and model performances are given in the work of *Sugi et al.* [1990, 1995].

[7] Before coupling the AGCM with the OGCM, the individual components are run in stand-alone mode to obtain appropriate initial conditions. The AGCM is integrated for nine months from 1 April 1988 to 1 January 1989 using the climatological SST [*Bottomley et al.*, 1990] as the boundary condition. The OGCM is spun up for 10 years from a state of rest using surface forcing derived from the climatological monthly mean wind stress and the surface temperature and salinity [*Levitus*, 1982]. The annual mean temperature and salinity fields [*Levitus*, 1982] are used at all levels as the initial condition at the beginning of the spin-up.

[8] After obtaining the required initial conditions, the AGCM and OGCM are coupled. In the coupling procedure, the AGCM is run for a day with a time step of 300 s, while the daily averaged wind stress, surface heat flux, and precipitation minus evaporation values are used to force the OGCM. The OGCM is run for a day with a time step of 900 s. Daily averaged SST values are computed to force the AGCM for the next day.

[9] The CGCM is integrated for 59 years. Data sets excluding the first 10 years are used in this analysis. This is because the simulated SST is not in equilibrium during the first 10 years. In this paper, we define anomalies as departures from the monthly averaged values taken over the final 50 years. Before the analyses, we trimmed the anomalies using a bandpass filter with a window from five months to seven years. This is done in order to retain the interannual modes while removing all other scales of variability in the anomalies.

[10] In the heat budget discussed in section 4, the surface heat flux that contributes to the mixed-layer temperature tendency $dT/dt$ averaged in the budget volume $V$ is integrated in the area $S$ surrounding a pole. It is calculated as

$$F = \frac{1}{\rho C_p}\frac{\int_S Q dS}{V} = \frac{1}{\rho C_p}\frac{\int_S Q dS}{hS}, \quad (1)$$

where $\rho$ (1.025 g/cm$^3$) is the density, $C_p$ is the specific heat capacity at constant pressure (we assume $\rho C_p \sim 1$), $Q$ is the model flux parameter and $h$ is the depth of the budget domain. We adopt $h$ = 85 m; this corresponds to the maximum value of the seasonally varying mixed-layer depth.

## 3. Analysis Results

### 3.1. Model Climatology

[11] This section discusses the model seasonal climatology. The climate conditions for SST and precipitation rate during austral summer (December–February) are shown in Figure 1. The SST is warmer near the equator and its gradient becomes strong in the subtropical region to the south of 30°S. We also notice that the isotherms of 28°C or less exhibit a southwest (SW)-northeast (NE) tilt with warmer water to the west of the basin between 30°S–20°S. Consistently the intertropical convergence zone (ITCZ) also exhibits a SW-NE tilt. Because of this structure of the ITCZ, eastern equatorial (southern) Africa receives good amount of seasonal rainfall during the austral spring and fall (austral summer). Though we notice a slight overestimation in the amount of model rainfall, the overall spatial structure of the simulated ITCZ agrees well with observations (not shown). The ITCZ penetrates into Kenya

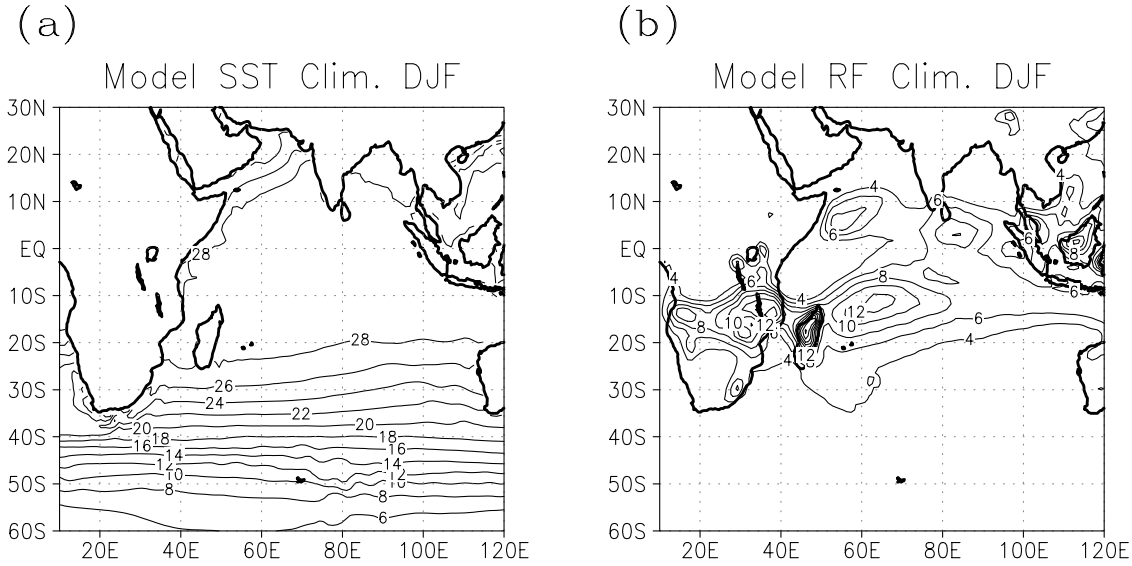


**Figure 1.** The austral summer climatological (a) SST pattern (contour interval is 2.0°C) and (b) precipitation rate (contour interval is 2.0 mm/day) in the Indian Ocean.

and northern Tanzania from the central Indian Ocean in October and November. From December to February it moves toward central Mozambique with the northwestward swing to the secondary convergence zone stretching from Angola to southern Congo.

[12] The interannual variability of the rainfall depends on the position and strength of the ITCZ. The model climatology for the SST and rainfall are in good agreement with observations (figure not shown). We note, however, that the model shows higher SST values in the tropical region and higher precipitation rates over southeast Africa.

[13] The seasonal evolution of the SLP and wind from October to March is shown in Figure 2. The Mascarene high and the corresponding anticyclonic circulation are located between 40°S–30°S. This high SLP plays a key role in the climate in the surrounding regions in the southern subtropical Indian Ocean. It may be noticed that the wind on the eastern side of the high is stronger between 30°S–20°S, which is consistent with cooler SST there as seen in Figure 1. Therefore, as noted by BY, the interannual movement of the Mascarene high is important for the IOSD formation.

### 3.2. Indian Ocean Subtropical Dipole Mode Events

[14] First, the raw SST anomalies have been inspected visually to confirm the presence of IOSD events in the CGCM simulation. This analysis has identified several positive and negative dipole events in the 50-year record. Typical examples are shown in Figure 3.

[15] In order to show the interannual evolution of IOSD, we have calculated a subtropical dipole index (SDI) based on the SST anomaly difference between the southwestern part and the southeastern part in the subtropical Indian Ocean. The two regions used for deriving the SDI are the rectangles 50°E–80°E, 42°S–30°S (the western part) and 75°E–105°E, 29°S–17°S (the eastern part). As discussed earlier, these regions are introduced based on a visual inspection of the raw data. Figure 4 shows the normalized (by the standard deviation) SDI thus obtained. We define a subtropical dipole event when the absolute SDI value exceeds one standard deviation. We exclude events which do not satisfy this condition during whole austral summer (DJF) to obtain clear composites. On the basis of this classification, we find 8 positive events (model years 18, 22, 32, 37, 38, 46, 50, 51) and 8 negative events (model years 15, 20, 23, 25, 40, 43, 52, 57). It may be noted that an event year here refers to the year during which evolution begins; the events actually reaches their mature stage in the beginning of the following year.

[16] The model IOSD peak is locked to the austral summer, which is consistent with observations. A qualitative agreement is also found between the statistics of the observed (as in BY) and the simulated SDI. Figure 5 shows the magnitude and duration of each event derived from the CGCM and GISST2.3b [*Rayner et al.*, 1996] data sets. The CGCM data set shows approximately the same frequency as that of the 42 years (1958–1999) observational data set that shows 8 positive events and 8 negative events. The averaged amplitudes of the SST dipole derived from the CGCM are similar to that from GISST for both positive and negative events. The averaged duration of positive events is very similar in the two data sets, but the negative events in the CGCM last a couple of months longer. Therefore, on the whole, we conclude that the CGCM does produce IOSD events that have characteristics comparable to those in the observational data.

[17] To see the spatial evolution of the model dipole events, we make composites of anomalies of SST, wind, latent heat flux, SLP and precipitation derived from the model simulation. Figure 6 shows those composites of the SST anomalies for the positive IOSD event. Here "(−1)"and "(0)" refer to the year when evolution begins and the mature phase, respectively. The anomalous dipole pattern is already seen in September (−1) and it evolves gradually and reaches the peak phase in January (0). As noted in the work of *Qian et al.* [2002], the amplitudes of the SST anomalies in the western pole are larger than in the

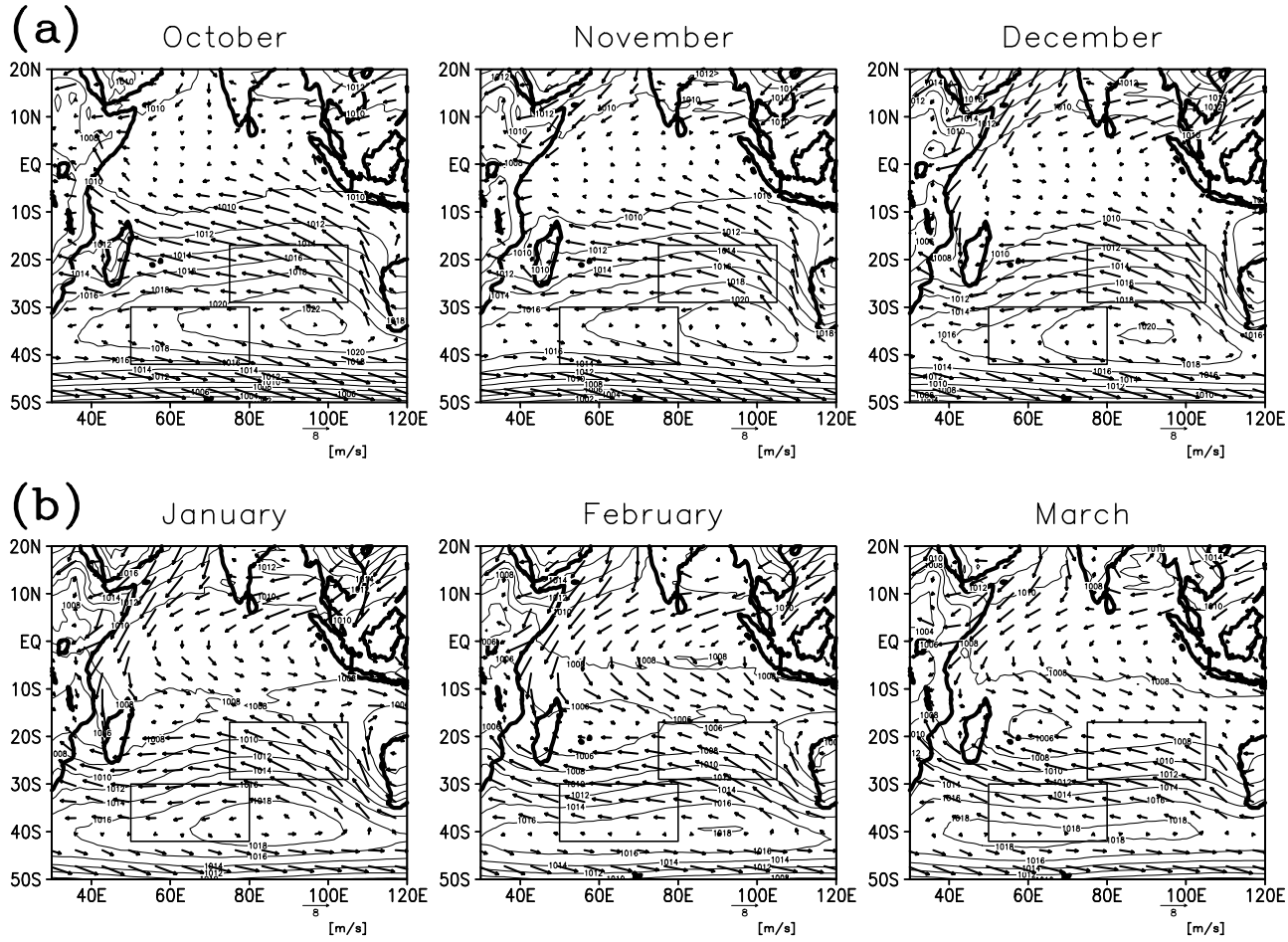


**Figure 2.** The austral summer climatological sea level pressure (solid lines) and surface wind (arrows) (a) from October to December (corresponds to the growing phase of IOSD as discussed later) and (b) from January to March (the mature and decaying phase of IOSD). The boxes indicate the positions of the two poles of IOSD.

eastern pole. For convenience, "IOSD growing phase" denotes the period until and including December (−1) and "IOSD decaying phase" denotes the period including and after January (0). The SST anomaly composite for the negative IOSD events also shows a similar evolution (Figure 7).

### 3.3. Origin of the Subtropical Dipole Mode

[18] To understand the formation of the subtropical dipole mode, we have prepared the composites of the SST tendency anomaly (Figure 8a) and the latent heat flux anomaly (Figure 8b) for positive IOSD events. The SST tendency anomaly in month $n$ ($STDA(n)$) is calculated using the SST anomalies ($SSTA$) in months $n + 1$ and $n - 1$ as

$$STDA(n) = \frac{SSTA(n+1) - SSTA(n-1)}{2}.$$

Interestingly, the two poles of the flux anomaly correspond well to those of the SST tendency anomaly. The negative (positive) SST anomaly is related to latent heat loss (gain): the eastern pole is cooled by the anomalous heat loss and the western pole is heated owing to less heat loss during the IOSD growing phase. After January (0), however, the situation reverses: the eastern pole is heated gradually, while the cooling in the western pole begins at the western side and extends eastward with time.

[19] Those latent heat flux anomalies are associated with surface wind anomalies (Figure 2). In the growing phase, a large positive SLP anomaly around 45°S (Figure 9a) signifies the southward migration as well as intensification of the Mascarene high. This positive SLP anomaly is associated with anomalous southeasterlies over the eastern pole and anomalous easterlies over the western pole of SST anomalies. The seasonal wind pattern associated with the Mascarene high in the region shows southeasterlies over the eastern pole and westerlies over the southern part of the western pole (October–December in Figure 2a). Therefore the anomalous wind associated with the SLP anomaly intensifies (weakens) the seasonal winds over the eastern pole (western pole). Because of the enhanced (weakened) evaporation, this leads to increase (decrease) of latent heat loss.

[20] The warm anomaly persisting on the western side, however, leads to the development of a negative SLP anomaly there (Figure 9b) [see also *Reason and Mulenga*, 1999; *Reason*, 2002]. The associated anomalous southeasterlies act to intensify the seasonal wind in the northwestern

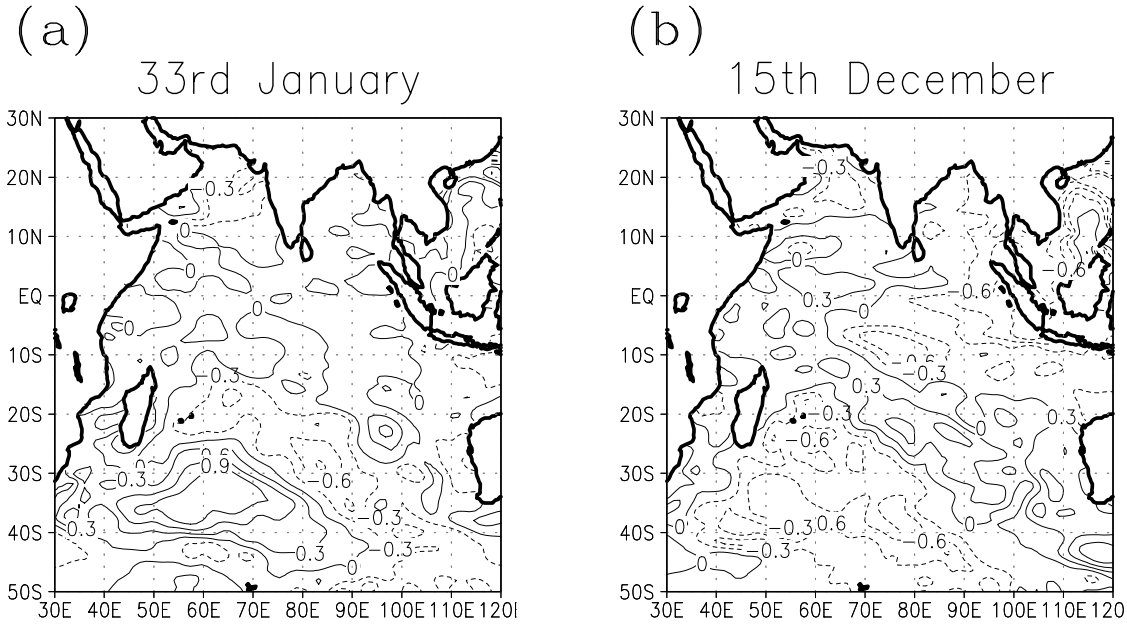


**Figure 3.** Examples of SST anomalies for (a) a positive IOSD event during January of the 33rd model year and (b) a negative IOSD event during December of the 15th model year. Contour interval is 0.3°C.

part of the western pole (Figure 2b, January–March), leading to a latent heat loss. The negative SLP anomaly weakens as the SST becomes colder. Therefore, as the western pole is cooled from the western side, the negative SLP anomaly disappears from the western side. This is accompanied by the motion and extension of the negative SLP anomaly toward the east. It decays eventually when the western pole composed of the warm SST anomaly disappears. Over the eastern pole, the anomalous southeasterlies which existed in the growing phase disappear. Anomalous northerly winds associated with the negative SLP anomaly appear in the decaying phase. The anomalous northerly winds weaken the seasonal southeasterlies and the associated latent heat loss; the eastern cool pole begins to warm up. Thus the IOSD is terminated by the SLP anomaly which appears in the latter phase owing to air-sea interaction.

[21] For the case of negative IOSD composites basically same features are seen but with the opposite sign. We show the SST tendency anomaly, the latent heat flux anomaly, the SLP anomaly and the wind anomaly for November (−1) and March (0) (Figure 10). Those months are representative of the growing and decaying phases. By November (−1), the negative SLP anomaly becomes apparent around 45°S accompanied by cyclonic wind anomalies at the surface. The positive SLP anomaly generated over the mature western cold pole (Figure 10c; March (0)) extends eastward. The anomalous westerlies (southeasterlies) in the western (eastern) pole act to weaken (intensify) the climatological wind field (not shown). Two differences, however, are found between the positive and negative IOSD formation: one is that the negative SLP anomaly of the negative IOSD is located farther south than the positive SLP anomaly of the positive IOSD. This may lead to an asymmetry between the positive and negative IOSD events. The other is that the mature phase of the negative IOSD persists for 4 months from January (0) to April (0), one month longer than the positive IOSD. The anomalous SLP and wind patterns that terminate the negative IOSD begin in May (0). We suggest that the weaker air-sea interaction over the colder western pole slows down the decay of the system.

[22] The composites of precipitation rate associated with positive IOSD events are shown in Figure 11. From around October (−1), an enhanced rainband extends from the southern Indian Ocean into Madagascar and Mozambique. Two enhanced rainbands extend from Mozambique to

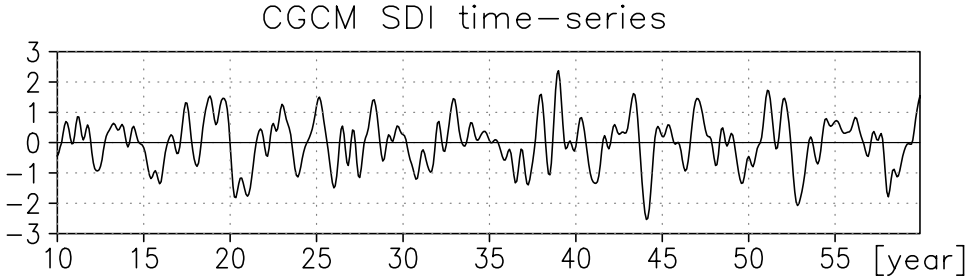


**Figure 4.** Simulated SDI time series during 50 years.

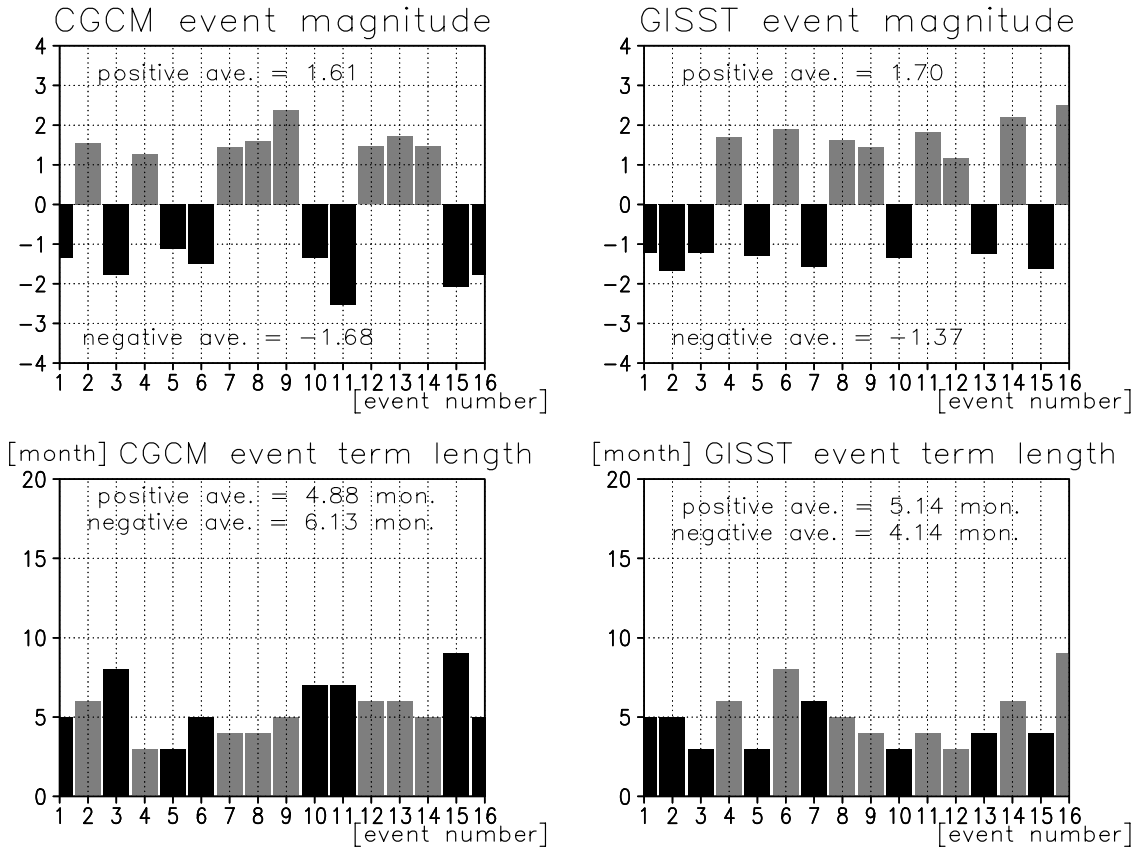


**Figure 5.** Histograms for comparing the characteristics of observed IOSD events in (right) GISST with simulated events in (left) CGCM. Bars shaded with gray denote the positive events and black bars the negative events. The "event number" shown on the abcisa is in order of occurrence. The top two panels show peak value of SDI for each event. The bottom two panels show duration of each event in which the absolute value of SDI is greater than 1.

Zambia and from Mozambique to South Africa during February (0) and March (0). This enhanced precipitation pattern is consistent with the numerical results from an atmospheric model by *Reason* [2002] for Africa and the observational results by *Qian et al.* [2002] for Africa and Indian Ocean basin. We note that the rainbands in Figure 11 intrude further south into southeastern Africa in February (0) and March (0) than the previous studies. The warmer than normal SST gives rise to enhanced storm activity in the midlatitude Indian Ocean. This is related to the cyclone which ultimately terminates the IOSD.

[23] The precipitation composites also suggest an intensification of the ITCZ in the central Indian Ocean during the growing phase of IOSD. The anomalous latent heat flux and the wind anomalies in the region suggest moisture convergence in the central Indian Ocean. This can explain the enhanced precipitation.

[24] The negative composites show precipitation patterns which are opposites of the positive patterns in some regions (Figure 12). During negative events, precipitation is reduced in the region from northern Mozambique to Zambia in January (0) to March (0). The well-defined rainband observed southeast of Madagascar during the positive events is absent owing to the colder SST there. The ITCZ in the central Indian Ocean is also weakened. We notice, however, that the precipitation in southeastern Africa is nonlinear and it is not very sensitive to SST anomalies related to IOSD events (Figure 12).

## 4. Discussion

[25] The time sequence of ocean-atmosphere anomalies in section 3.3 clearly shows an atmospheric influence on SST variability through changes of the surface heat fluxes during the growing phase of the IOSD. It remains uncertain, however, how the subtropical SST dipole reinforces the SLP anomaly that in turn drives the SST anomaly. The present analysis shows that the atmosphere responds to changes of the underlying SST in the later stages of the IOSD evolution. This is well-depicted in a zonal cross section of a composite of the tropospheric geopotential anomaly averaged between 45°S–35°S for positive IOSD events (Figure 13). From September (−1), at the beginning of the positive IOSD event, the positive geopotential anomaly shows an equivalent barotropic structure. As the structure strengthens, it starts to show a baroclinic structure in December (−1). A similar but opposite structural change is apparent in the negative composite (Figure 14). The equivalent barotropic structure of the initial atmospheric anomalies indicates that the IOSD event may be triggered by remotely forced stationary Rossby wave trains propagating into the southern Indian Ocean. The disturbances may be

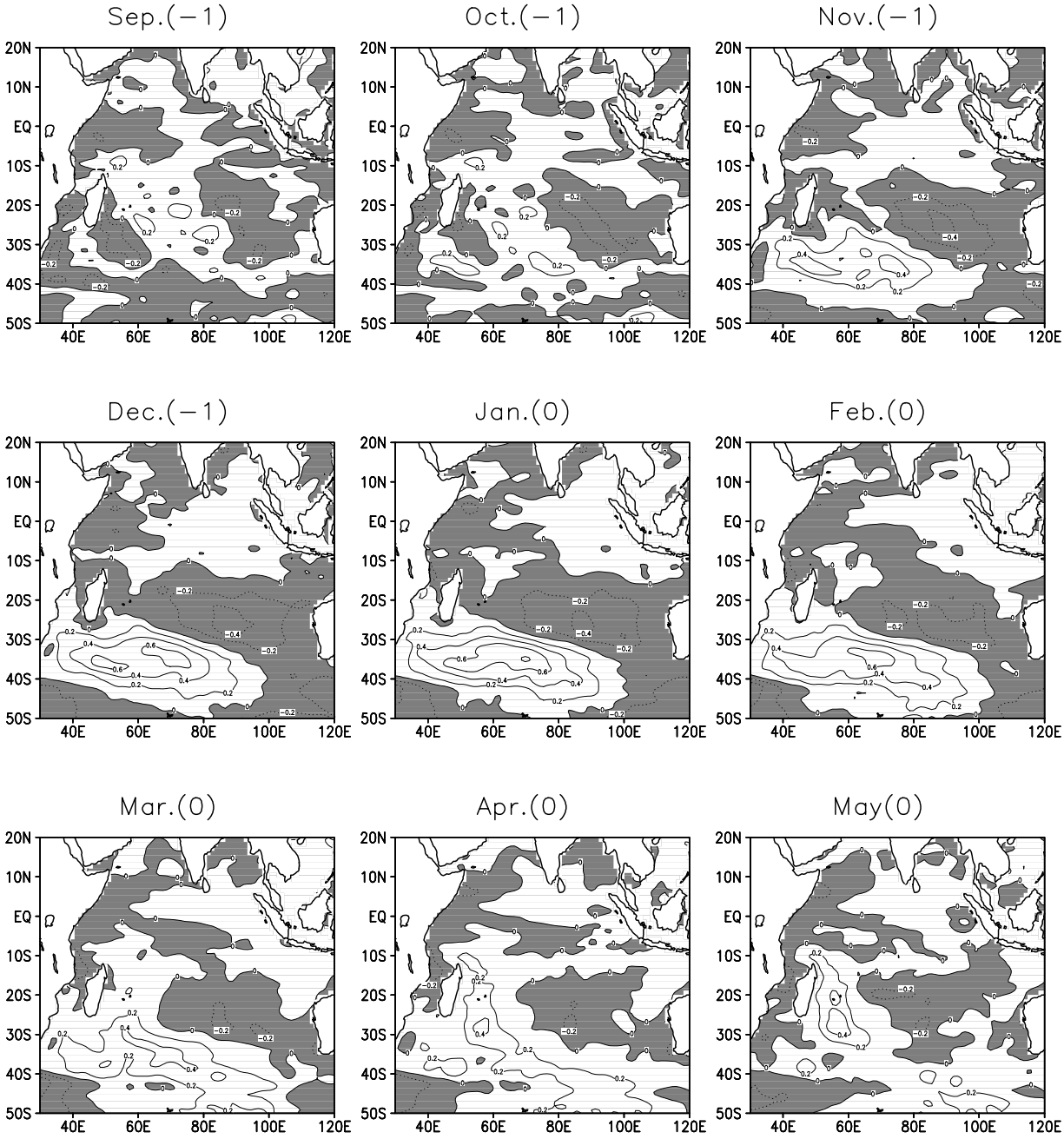


**Figure 6.** Monthly composites of SST anomalies for eight positive IOSD events (model years 18, 22, 32, 37, 38, 46, 50, and 51) from September in the evolution year to the next May. Contour interval is 0.2°C. Negative anomalies are shaded.

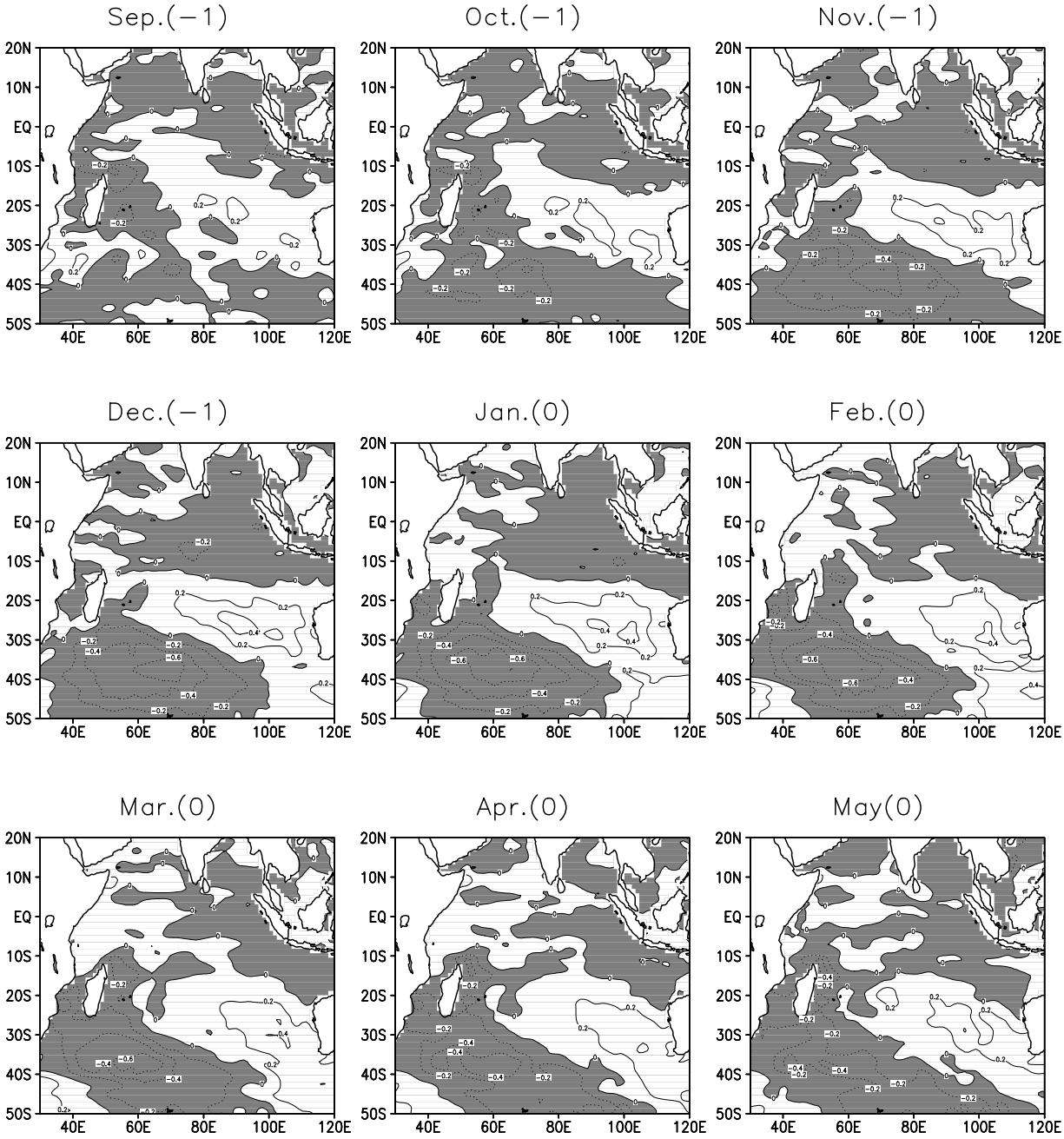


**Figure 7.** Same as in Figure 6 except for eight negative IOSD events (model years 15, 20, 23, 25, 40, 43, 52, and 57).

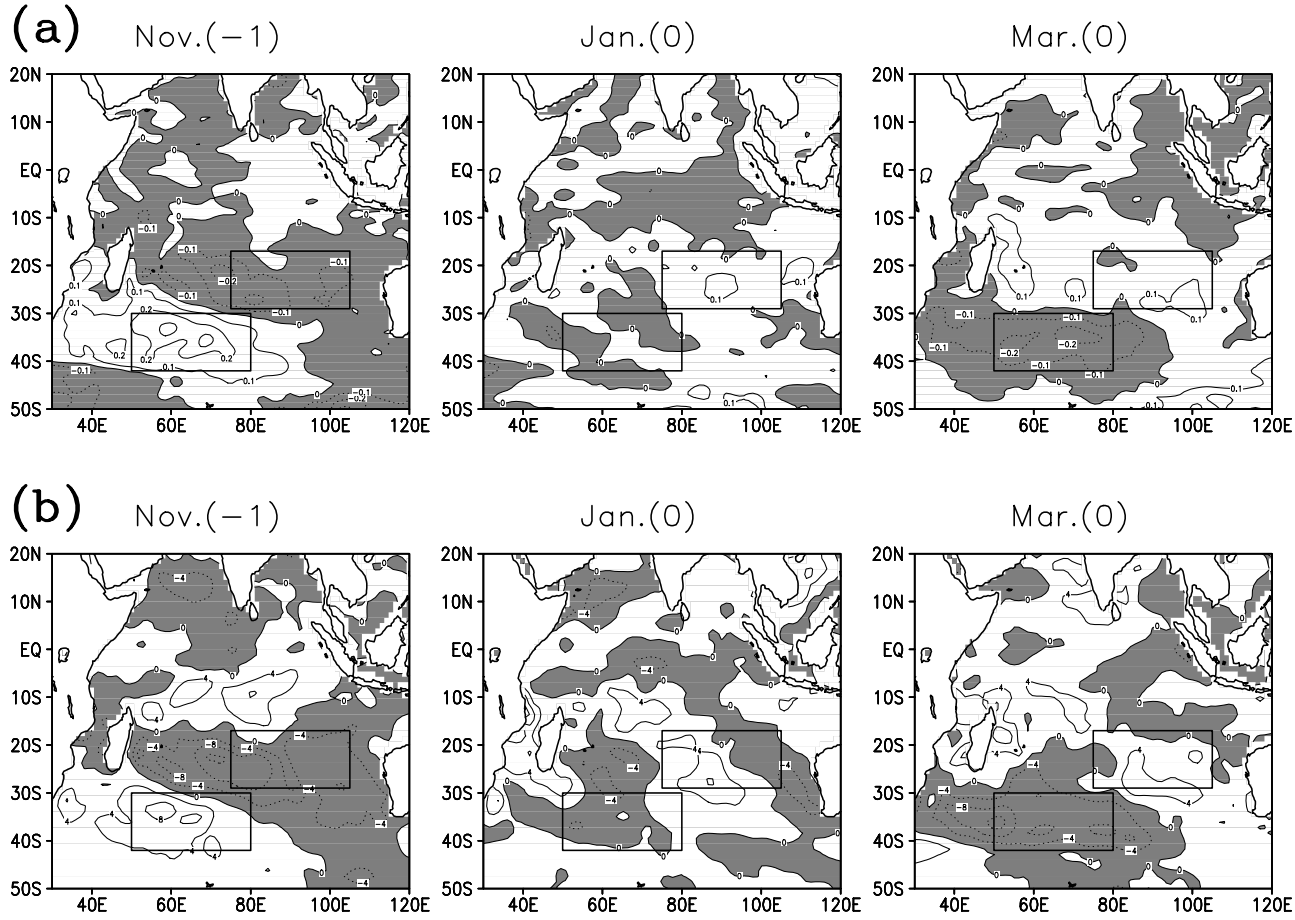


**Figure 8.** Monthly composites for eight positive IOSD events in November (−1), January (0), and March (0) of (a) SST tendency anomalies and (b) latent heat flux anomalies. Contour interval is 0.1°C in Figure 8a and 4.0 W/m$^2$ in Figure 8b, respectively. Negative anomalies are shaded. The boxes display the positions of the two poles of SST anomalies.

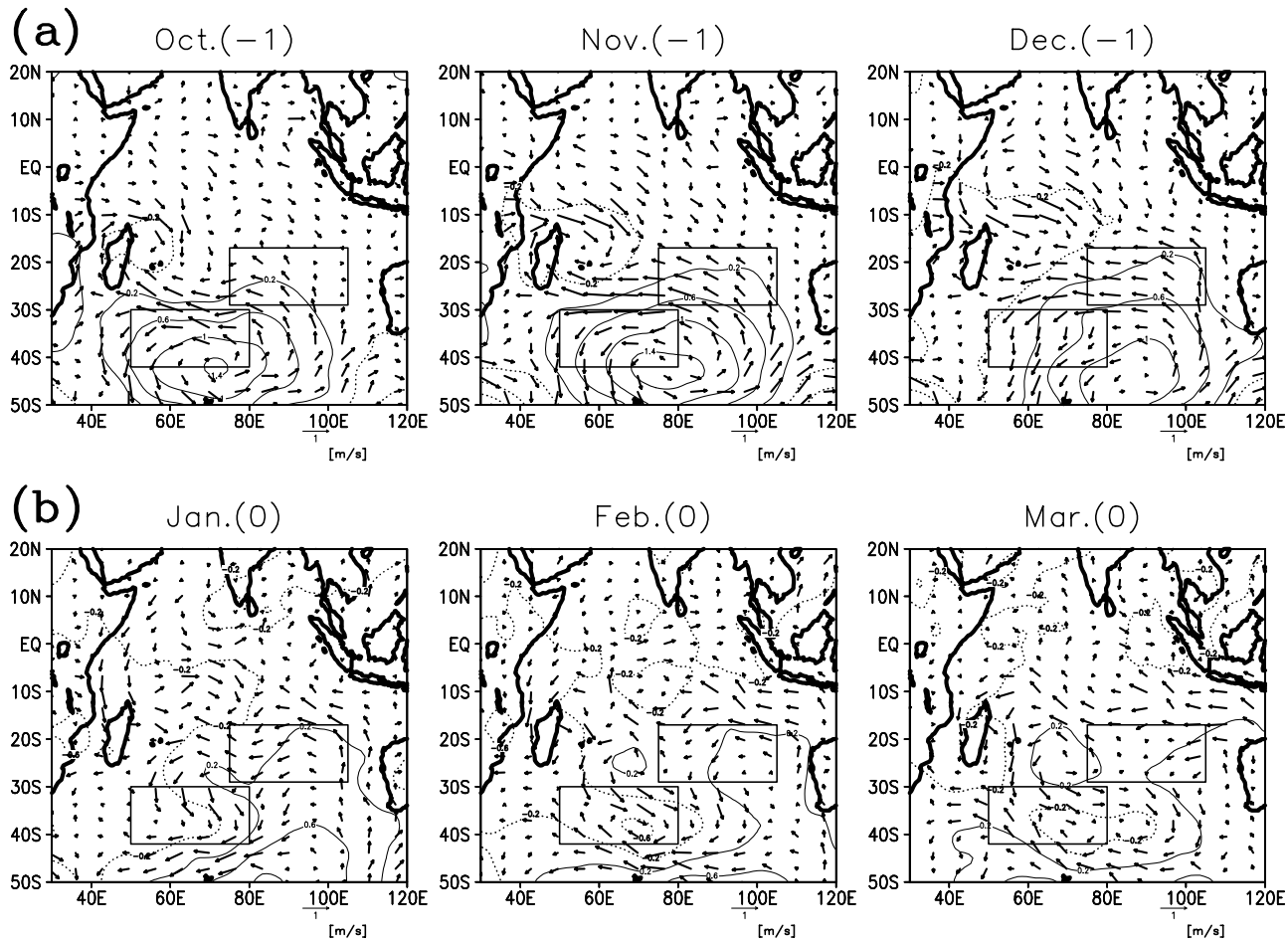


**Figure 9.** Monthly composites of SLP anomalies (contours) and wind (arrows) anomalies for positive IOSD events (a) during the IOSD growing phase, from October (−1) to December (−1) and (b) during the IOSD decaying phase, from January (0) to March (0). For SLP anomalies, the positive values are expressed with solid lines and the negative values with dotted lines. Contour interval is 0.4 hPa. The boxes display the positions of the two poles of SST anomalies.

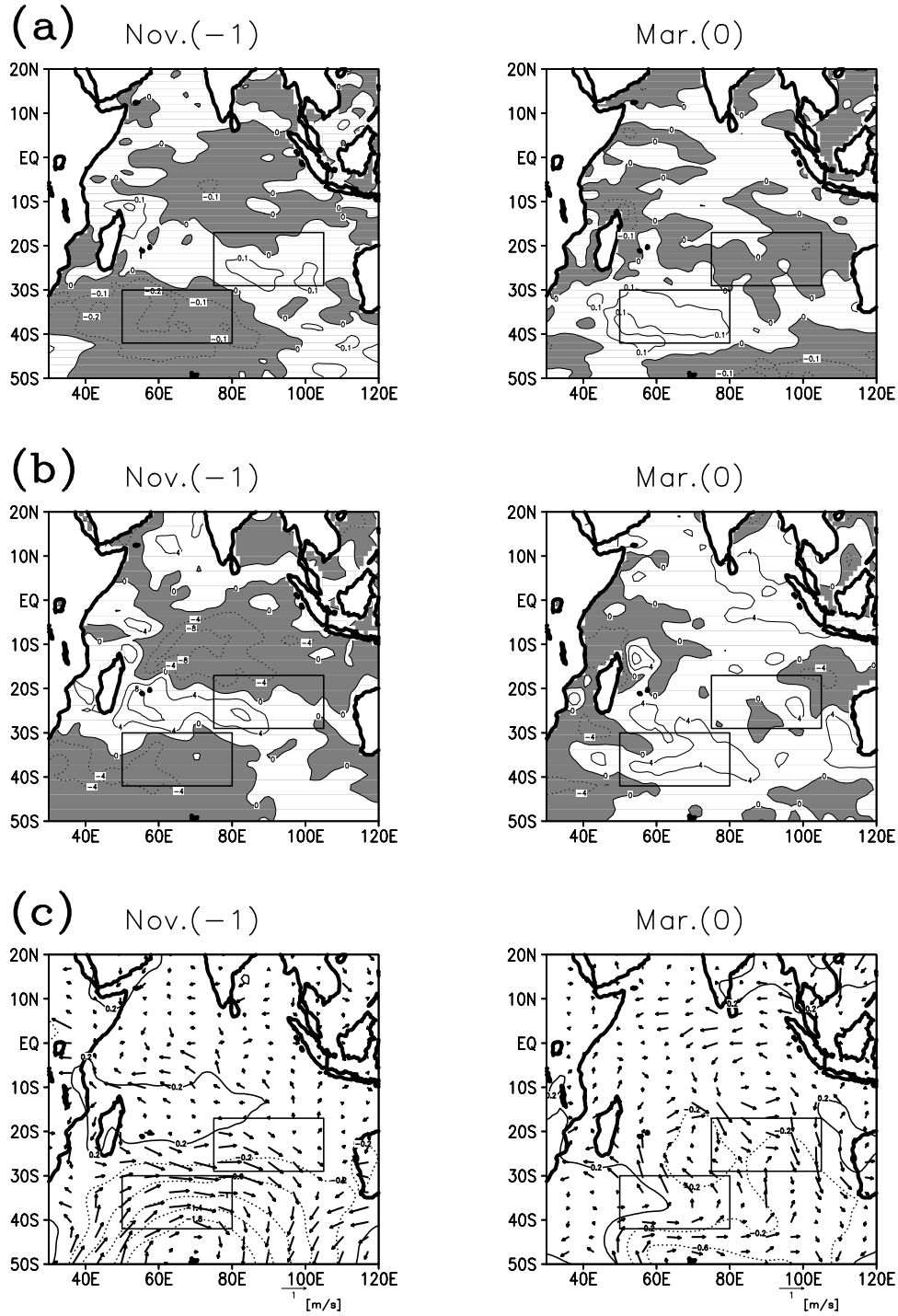


**Figure 10.** The composites of the negative IOSD events in November (−1) and March (0) for (a) SST tendency anomaly, (b) the latent heat flux anomaly, and (c) SLP and wind anomaly. Contour intervals are 0.1°C, 4.0 W/m$^2$ and 0.4 hPa, respectively.

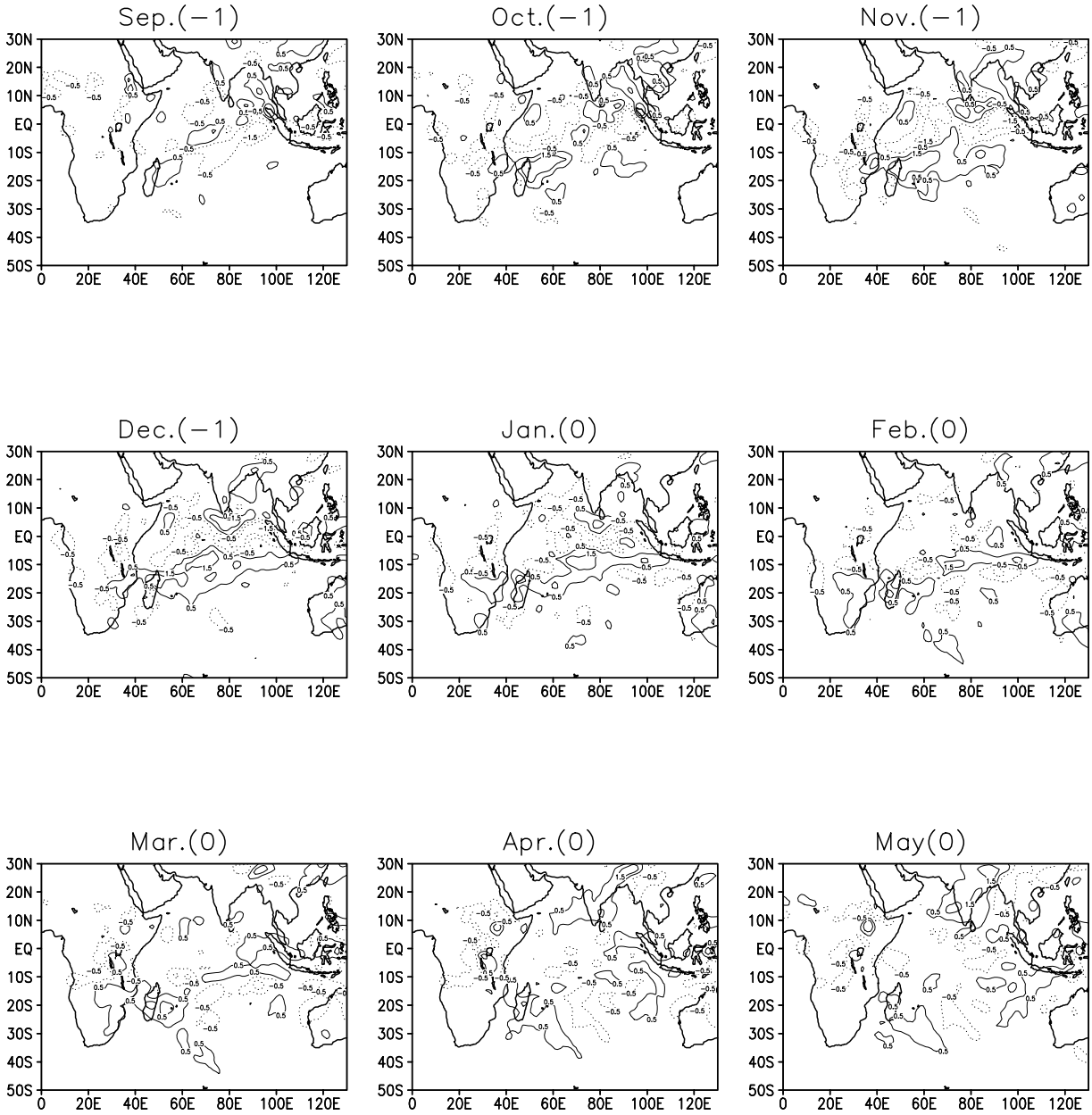


**Figure 11.** The anomalous precipitation composites of positive IOSD events. Contour interval is 1.0 mm/day. The negative values are expressed with dotted line.

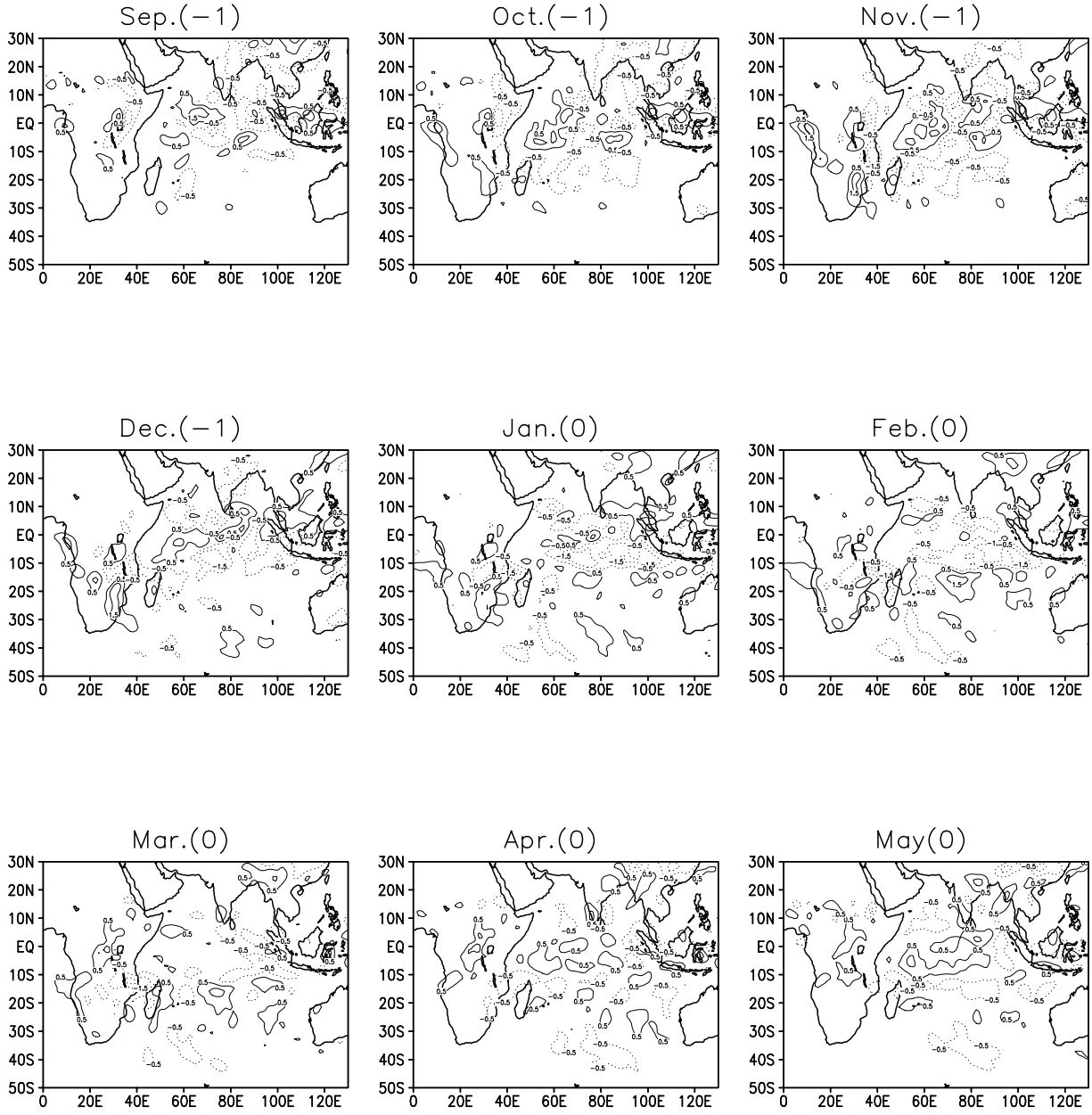


**Figure 12.** Same as in Figure 11 except for the negative IOSD events.

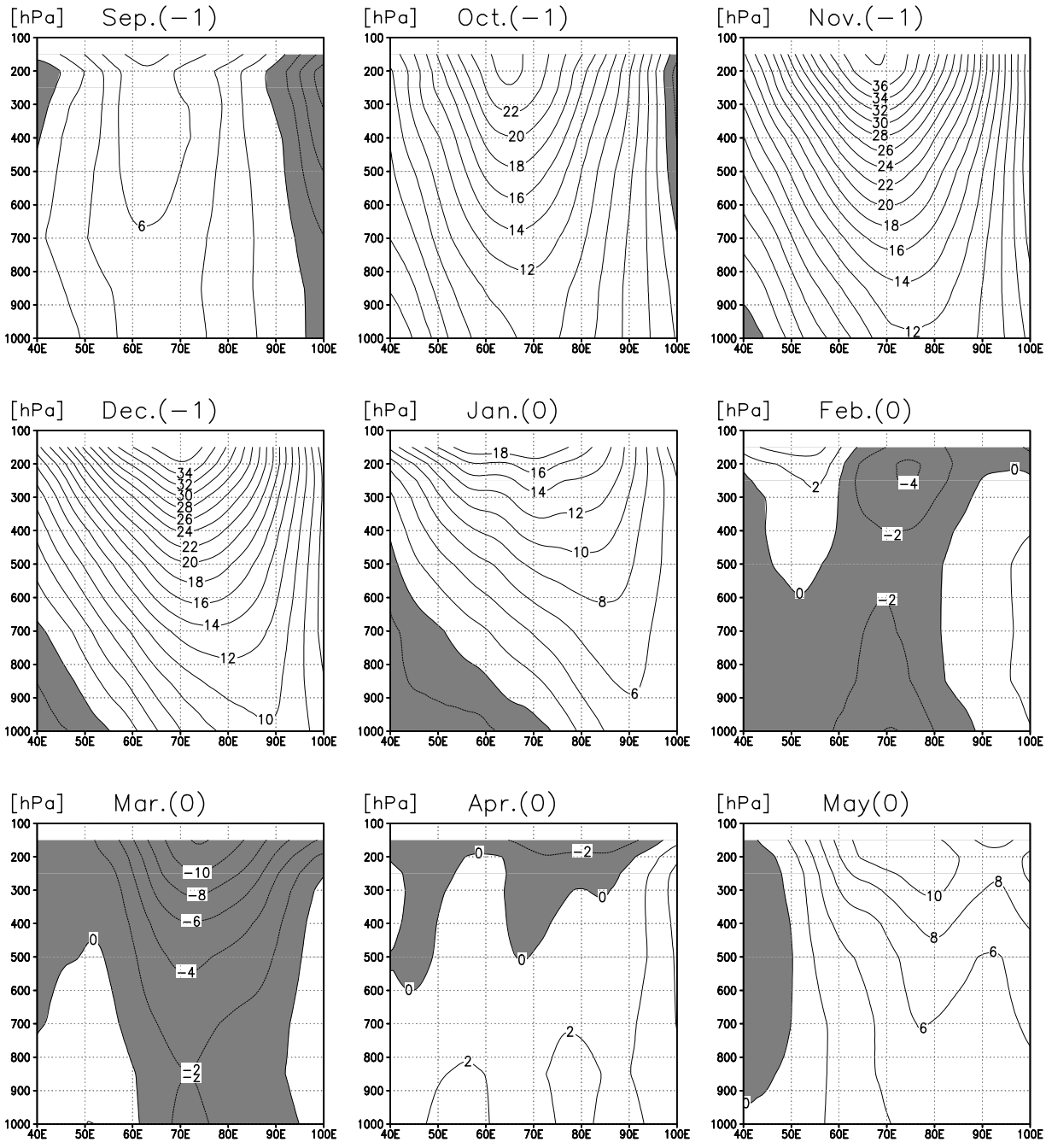


**Figure 13.** Zonal cross sections of tropospheric geopotential height composite anomalies of positive IOSD events averaged between 45°S–35°S. Contour interval is 2.0 m. Solid lines denote positive values and dashed lines denote negative values.

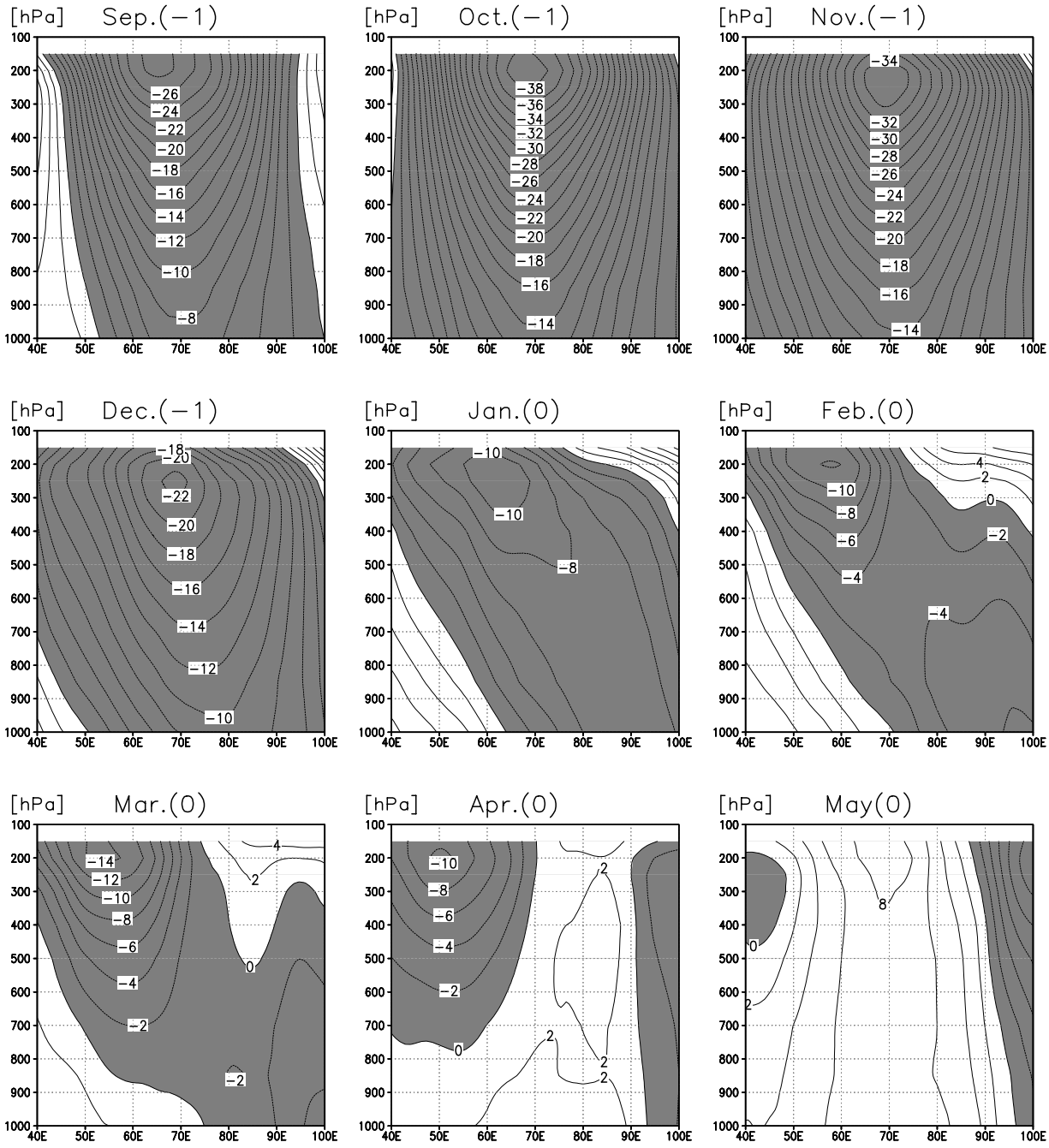


**Figure 14.** Same as in Figure 13 except for the negative IOSD events.

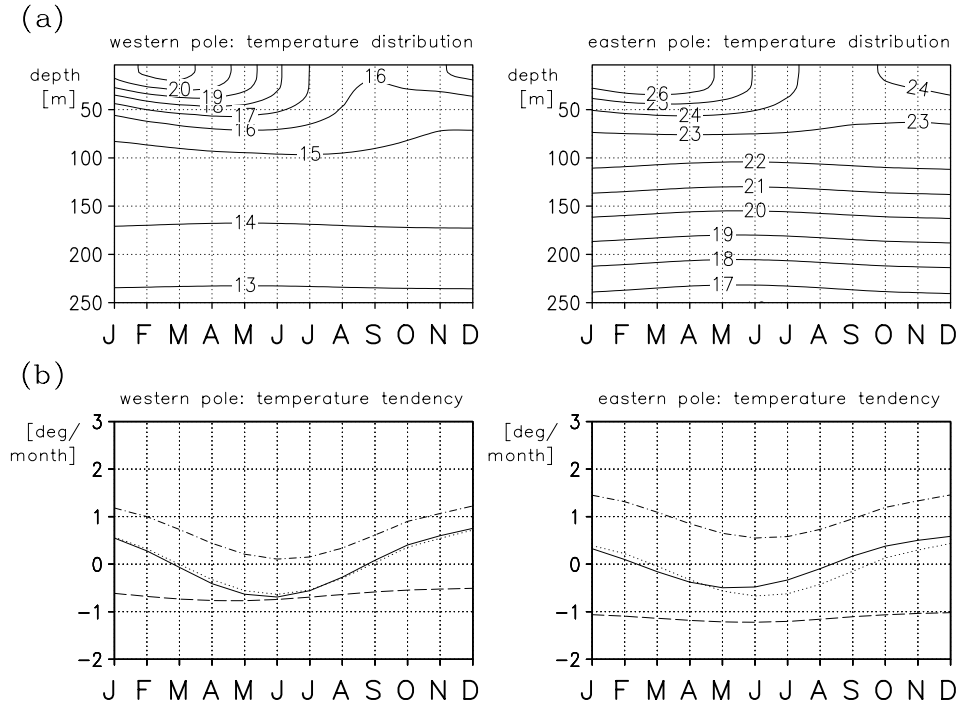


**Figure 15.** (a) The seasonal evolution of upper ocean temperature in the vertical section averaged inside the western pole region (left panels) and the eastern pole region (right panels). The unit is °C. (b) The temperature tendency (solid lines), surface heat flux (dotted lines), latent heat flux (dashed lines), and solar radiation flux (dashed dotted lines) in the upper 85 m of the western pole region (left panels) and eastern pole region (right panels).

trapped and intensified over the SST anomaly. The initial growth of the atmospheric component of IOSD needs further investigation.

[26] An interesting question arises: why does SST respond in a particular season to change of the Mascarene high? One factor is the significant change of the seasonal wind field around the western pole. Since the seasonal winds in the southern region of the western pole change from northwesterlies to southeasterlies around January as the Mascarene high shifts southward (see Figure 2), the suppressed latent heat loss by the anomalous easterlies during the IOSD evolution cannot hold after January (0) (see Figure 9a). The other factor lies in the subsurface condition. The ocean mixed ayer tends to be shallow during the austral summer because of relatively calm conditions and strong insolation. Anomalous surface heat flux of a given intensity should lead to larger anomalies in a shallower mixed layer. The seasonal march of climatological temperature and the contribution of the heat flux to the temperature tendency within the two poles are shown in Figure 15. The figure indicates the seasonal variations of the mixed-layer depth which is deeper in the austral summer and shallower in the austral winter (Figure 15a). The seasonal change of the temperature tendency averaged in the upper 85 m (Figure 15b) is compatible with that of the mixed-layer depth, and it changes sign from positive to negative in February, and from negative to positive in August. We note that the actual temperature tendency is almost equal to the seasonal variation of the surface heat flux, which is calculated using equation (1). This surface heat flux is decomposed into the latent heat flux and the solar radiation flux in this figure. Since the latent heat flux is almost constant throughout the year, the heat flux variability is mainly due to the seasonal solar radiation change. We may thus conclude that the seasonal temperature and the mixed-layer structure are basically determined by the insolation. The continuous heat flux changes due to atmospheric variability will therefore eventually cause the changes in the SST and the upper layer heat content.

[27] The anomaly composites for positive IOSD events are shown in Figure 16. In January (0), the anomalously warm (cold) water in the western (eastern) pole reaches a maximum (Figure 16a). The western pole begins to warm in April (−1), and starts to cool in January (0). The change of the latent heat flux basically determines the temperature tendency; the anomalous weakening of the latent heat flux from the ocean leads to the warming in the surface layer. The eastern pole starts cooling in January (−1) and the cooling reaches the maximum in January (0). The temperature tendency is also dominated by the change of the latent heat flux in the growing phase starting around May (−1). Similar features are obtained for the negative case (see Figure 17).

[28] Two components of the heat flux contribute to the IOSD formation. One is the insolation, which is the cause of the shallow seasonal mixed-layer depth in the austral summer. The other is the interannual variability of the latent heat flux, which is responsible for the interannual IOSD

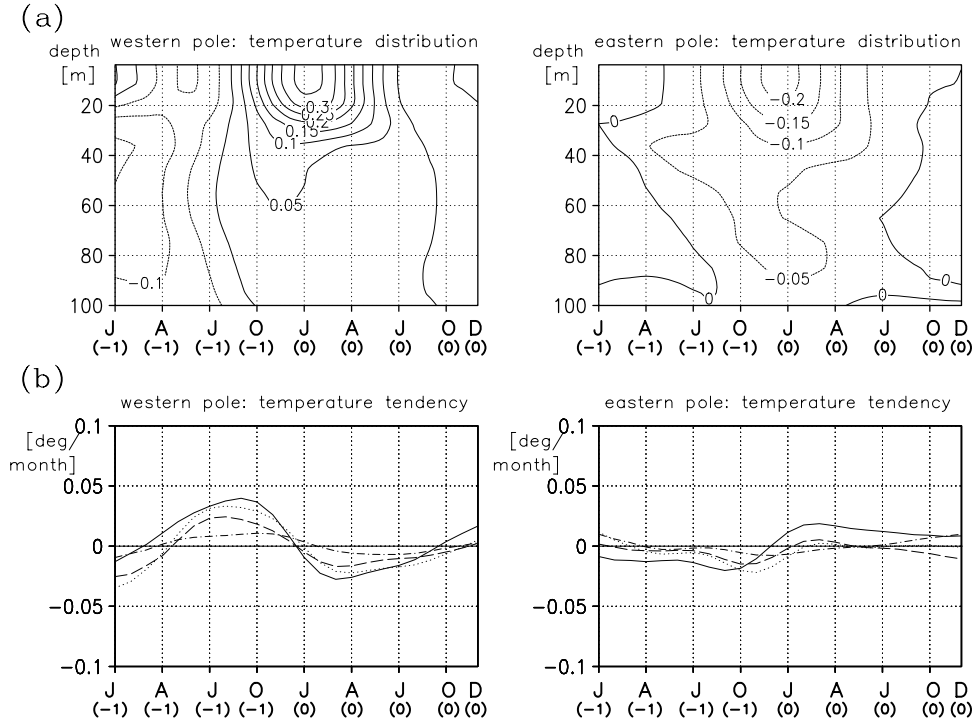


**Figure 16.** Same as in Figure 15 except for the composite anomalies of the positive IOSD events. The horizontal axis is marked at 3 month intervals.

events. The IOSD event starts in late austral fall of the previous year and peaks during the austral summer when the depth of the seasonal mixed layer becomes shallowest.

[29] The latent heat flux contributes to the IOSD formation for a period of about nine months, from May (−1) to January (0). We cannot explain why the heat flux anomaly lasts for nine months without a positive feedback mechanism between the atmosphere and ocean. *Qian et al.* [2002] also suggested the existence of such a positive feedback for the IOSD formation. Moreover, *Liu and Wu* [2004] have clarified from their model study that a warm SST forcing tends to generate a warm-ridge response, which indicates a

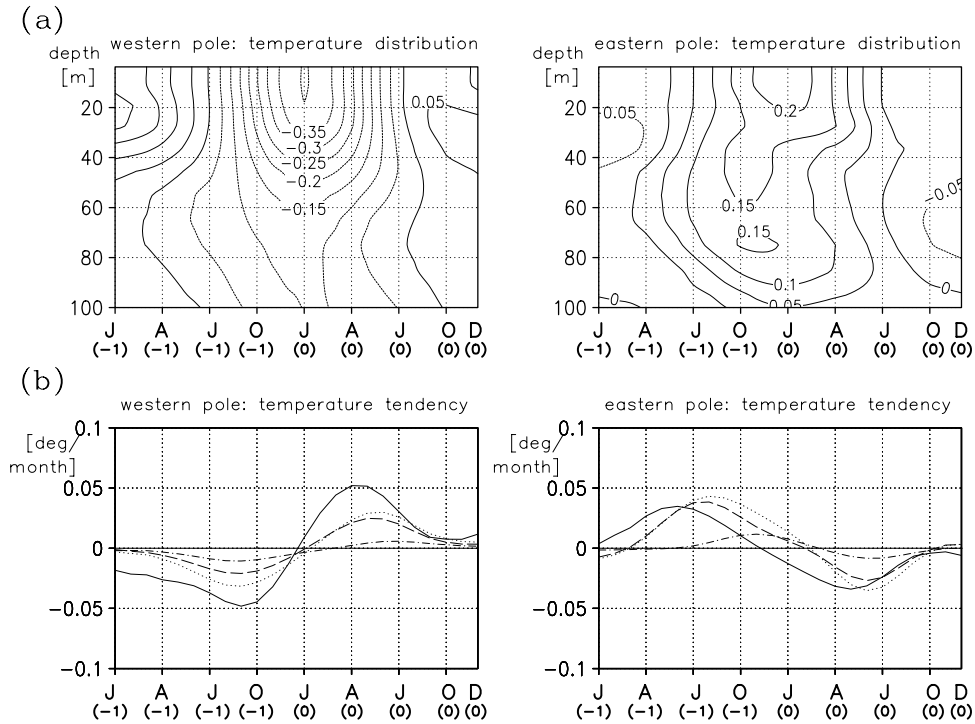


**Figure 17.** Same as in Figure 16 except for the negative IOSD events.

positive feedback between the warm pole and the anomalous high SLP.

[30] **Acknowledgments.** We thank Yukio Masumoto, Surya Rao, and Hisashi Nakamura for stimulating discussions during the course of this work. We also thank Gary Meyers for helpful suggestions and Tivon Jacobson for proofreading. The first author acknowledges financial support from the MEXT project RR2002 through Mitsubishi Heavy Industries, Ltd.

## References

Allan, R., J. Lindesay, and D. Parker (1996), *El Niño Southern Oscillation and Climatic Variability*, 416 pp., Commonw. Sci. and Indust. Res. Org., Melbourne, Vict.

Behera, S. K., and T. Yamagata (2001), Subtropical SST dipole events in the southern Indian ocean, *Geophys. Res. Lett.*, *28*, 327–330.

Bottomley, M., C. K. Folland, J. Hsiung, R. E. Newell, and D. E. Parker (1990), *Global Ocean Surface Temperature Atlas "GOSTA,"* 20 pp., UK Met Off., Bracknell, UK.

Ferreira, D., C. Frankignoul, and J. Marshall (2001), Coupled ocean-atmosphere dynamics in a simple midlatitude climate model, *J. Clim.*, *14*, 3704–3723.

Goddard, L., and N. E. Graham (1999), Importance of the Indian Ocean for simulating rainfall anomalies over eastern and southern Africa, *J. Geophys. Res.*, *104*, 19,099–19,116.

Hastenrath, S., A. Nicklis, and L. Greischar (1993), Atmospheric-hydrospheric mechanisms of climate anomalies in the western equatorial Indian Ocean, *J. Geophus. Res.*, *98*, 20,219–20,235.

Iizuka, S., T. Matsuura, and T. Yamagata (2000), The Indian Ocean SST dipole simulated in a coupled general circulation model, *Geophys. Res. Lett.*, *27*, 3369–3372.

Jury, M. R., D. B. Enfield, and J. L. Melice (2002), Tropical monsoons around Africa: Stability of El Niño-Southern Oscillation associations and links with continental climate, *J. Geophys. Res.*, *107*(C1), 3151, doi:10.1029/2000JC000507.

Katayama, A. (1972), A simplified scheme for computing radiative transfer in the troposphere, *Tech. Rep. 6*, Univ. of Calif., Los Angeles.

Kuo, H. L. (1974), Further studies of the influence of cumulus convection on large scale flow, *J. Atmos. Sci.*, *31*, 1232–1240.

Lacis, A. A., and J. E. Hansen (1974), A parameterization for the absorption of solar radiation in the Earth's atmosphere, *J. Atmos. Sci.*, *31*, 118–133.

Levitus, S. (1982), *Climatological Atlas of the World Ocean*, 173 pp., *NOAA Prof. Pap. 13*, U.S. Govt. Print. Off., Washington D. C.

Liu, Z., and L. Wu (2004), Atmospheric response to North Pacific SST: The role of ocean-atmosphere coupling, *J. Clim.*, in press.

Louis, J. F., M. Tiedtke, and J. E. Geleyn (1982), A short history of PBL parameterization at ECMWF, in *Proceedings of the Workshop on Planetary Boundary Layer Parameterization*, pp. 59–79, Eur. Cent. for Medium-Range Weather Forecasts, Reading, UK.

Mason, S. J. (1995), Sea-surface temperature—South-African rainfall associations, 1910–1989, *Int. J. Climatol.*, *15*, 119–135.

Nicholson, S. E., and J. Kim (1997), The relationship of the El Niño—Southern Oscillation to African rainfall, *Int. J. Climatol.*, *17*, 117–135.

Ogallo, L. J., J. E. Janowiak, and M. S. Halpert (1988), Teleconnection between seasonal rainfall over east-Africa and global sea-surface temperature anomalies, *J. Meteorol. Soc. Jpn.*, *66*, 807–822.

Pacanowski, R. C. (1996), *Documentation User's Guide and Reference (MOM2)*, 329 pp., Geophys. Fluid Dyn. Lab., Princeton, N. J.

Pacanowski, R. C., and S. G. H. Philander (1981), Parameterization of vertical mixing in numerical models of tropical oceans, *J. Phys. Oceanogr.*, *11*, 1443–1451.

Paulson, E. A., and J. J. Simpson (1977), Irradiance measurements in the upper ocean, *J. Phys. Oceanogr.*, *8*, 1572–1583.

Qian, W., H. Hu, Y. Deng, and J. Tian (2002), Signals of interannual and interdecadal variability of air-sea interaction in the basin-wide Indian Ocean, *Atmos. Ocean*, *40*, 293–311.

Rayner, N. A., E. B. Horton, D. E. Parker, C. K. Folland, and R. B. Hackett (1996), Version 2.2 of the global sea ice sea surface temperature data set, *Clim. Res. Tech. Note 74*, Hadley Cent. for Clim. Predict. and Res., Exeter, UK.

Reason, C. J. C. (2002), Sensitivity of the southern African circulation to dipole sea-surface temperature patterns in the south Indian Ocean, *Int. J. Climatol.*, *22*, 377–393.

Reason, C. J. C., and H. Mulenga (1999), Relationships between South African rainfall and SST anomalies in the southwest Indian Ocean, *Int. J. Climatol.*, *19*, 1651–1673.

Reason, C. J. C., R. J. Allan, J. A. Lindesay, and T. J. Ansell (2000), ENSO and climatic signals across the Indian Ocean basin in the global context: Part I, interannual composite patterns, *Int. J. Climatol.*, *20*, 1285–1327.

Ropelewski, C., and M. Halpert (1987), Global and regional scale precipitation patterns associated with the El-Niño southern oscillation, *Mon. Weather Rev.*, *115*, 1606–1626.

Saji, N. H., and T. Yamagata (2003), Possible impacts of Indian Ocean Dipole mode events on global climate, *Climate Res.*, *25*, 151–169.

Sugi, M., K. Kuma, K. Tada, K. Tamiya, N. Hasegawa, T. Iwasaki, S. Yamada, and T. Kitade (1990), Description and performance of the JMA operational global spectral model (JMA–GSM88), *Geol. Mag.*, *43*, 105–130.

Sugi, M., R. Kawamura, and N. Sato (1995), The climate simulated by the JMA global model part I: Global Feature, *Rep. 54*, Natl. Res. Inst. for Earth Sci. and Disaster Prev., Jpn. Meteorol. Ag., Tokyo.

Tiedtke, M. (1985), The sensitivity of the time-mean large-scale flow cumulus convection in the ECMWF model, in *Workshop on Convection in Large-Scale Numerical Models*, pp. 297–316, Eur. Cent. for Medium-Range Weather Forecasts, Bracknell, UK.

Walker, N. D. (1990), Links between South African summer rainfall and temperature variability of the Agulhas and Benguela current systems, *J. Geophys. Res.*, *95*, 3297–3319.

S. K. Behera, Institute for Global Change Research/Frontier Research Center for Global Change, 3173-25, Showa-machi, Kanagawa 236-0001, Japan.

S. Iizuka, National Research Institute for Earth Science and Disaster Prevention, Tsukuba, Ibaraki 305-0006, Japan.

R. Suzuki and T. Yamagata, Department of Earth and Planetary Science, The University of Tokyo, Room 810, New-1st building, 7-3-1, Hongo, Bunkyo-ku, Tokyo 113-0033, Japan. (suzuki@eps.s.u-tokyo.ac.jp)